

Percussion Device for Anomaly Detection in Soft Tissue

Bennet Cobley¹, Jacob Tan¹, Oliver Thompson¹ and Pilar Zhang Qiu¹

Abstract—Medical percussion, used in clinical examination, is a diagnostic procedure in which the chest, back and abdomen are tapped to determine the conditions of underlying tissues by the acoustic response. Although percussion is common in medical practice, there is a limited understanding of its dynamics. This paper studies the acoustic response of percussion and tests how a compliant mechanism might replicate the percussion action. We ran numerical simulations and conducted experiments using a mechanically actuated plexor to detect a hard nodule (representing a lipoma or cancerous lump) embedded in a silicone phantom at varying depths. We established that acoustic response varies with nodule depth. Nodule depths could be distinguished using wavelet transforms and using saliency maps from a convolutional neural network which was used to generate a predictive model. Our findings show that a nodule closer to the surface of the tissue model increases the damping factor and attenuates frequencies between 175 Hz and 400 Hz. These results, for the first time, provide design guidelines for how a robotic device and audio analysis might be used to aid or automate percussion examination.

I. INTRODUCTION

Medical percussion, used in clinical examination, is a diagnostic procedure in which the chest, back and abdomen are tapped to determine the conditions of underlying tissues by the acoustic response. It can be used to determine the presence of air, fluid or solid material. Percussion examination is a preliminary assessment to inform other diagnostic methods such as ultrasonic sonography, computed tomography and magnetic resonance imaging (MRI) [1]. While percussion is common in medical practice, it is not fully known what auditory attributes determine a diagnosis. A deeper understanding of the acoustic response of percussion will provide new insights into the design of a robotic device that might be used to aid or automate percussion examination. This has exciting future applications in that it might improve medical training, enable remote (video-link) patient examinations, or even increase the accuracy of percussion diagnoses.

The currently accepted percussion method is manual percussion. The left hand is fixed on the region to be assessed, with the middle finger isolated from the other fingers (Fig. 1 (a)). The middle finger of the right hand strikes the left and the examiner listens to the acoustic response [2]. Historically, devices have also been used to augment percussion methods. In the 18th century a percusor and pleximeter were documented (Fig. 1 (b)) and a stethoscope-attached handheld percussion device was patented in 2004 (Fig. 1 (c)).

The literature states that percussion examination is based on the difference in pitch between sounds elicited by tapping on the body wall. The audio response depends on the ease

¹This work was partly supported by an excellence in teaching innovation grant from Imperial College London

TABLE I
CHEST AND ABDOMINAL PERCUSSION ACOUSTIC RESPONSE
CHARACTERISTICS [4]

	Intensity	Tone (Pitch)	Thoracic Elasticity	Duration
Chest Percussion	Low Normal High	Low Normal High	Perceived by percussing finger	
Abdominal Percussion				Short Normal Long

with which the body wall vibrates and is influenced by underlying organs, strength of the stroke and state of the body wall [3]. Characteristics of the acoustic response combine to form percussion notes, as summarised in Table I. Three key percussion notes are resonance, tympany and dullness. Resonant sounds are low pitched and hollow; tympanic are long, high-pitch and loud; dull is short, low-pitch and quiet. Certain pathologies produce abnormal sounds that can be picked up by the examiner during percussion. For example, cases of emphysema and pneumothorax cause hyperresonance during chest percussion; large areas of dullness in the abdomen suggest an enlarged organ or a mass [4].

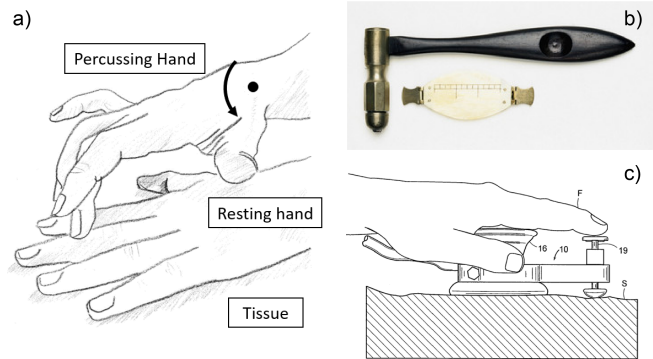


Fig. 1. Percussion methods and devices. (a) Manual Percussion [5]. (b) Percusor and Pleximeter [6]. (c) Stethoscope-attached percussion device [7]

The relationship between internal body structure and percussion has been studied. Rice [8] explored the transmission property of the chest by modelling the respiratory system as a coupled system with the chest wall and the lung placed in series. When struck with an external shock, the chest wall vibrates and 'rings' as a resonant cavity partially damped by the thoracic contents. McKusick [9] studied the acoustic response of chest percussion with sound spectrography. He found that the resonant note is composed by additional vibrations of the thorax, whereas the dull note features only higher frequencies as it is not weighted by the low-frequency vibrations of the thorax.

Mansy [10] analysed the acoustic response of abdominal

percussion by comparing the signal waveform for varying pneumoperitoneum conditions. The feedback was captured with a condenser microphone and analysed using signal spectrograms. The results showed significant differences in the frequency domain between moderate and severe pneumoperitoneum conditions.

The literature shows that auditory characteristics in percussion can be quantified in various specific cases and pathologies. Rice studied the chest and respiratory system, but the transmission property of the abdominal region is unknown. Mansy did not standardise the percussion action in experiments; it was applied manually, which could have resulted in noticeable variations in the force profile.

Acoustic response in percussion examination is an established area of interest in the literature but has not been studied in the context of modern technologies. A robotic device capable of delivering repeatable motion could remove force inconsistencies inherent in human actions, allowing us to focus on the relationship between the percussion action and acoustic response. This paper proposes new methods to quantitatively analyse the dynamics of abdominal percussion, and uses these insights to outline a design for a robotic percussion device that might be used to aid or automate percussion examination.

II. METHODS

Mathematical simulations were built using MATLAB to test various designs to replicate a human performing percussion. Firstly, a volunteer was asked to perform percussion on an Ecoflex 00-10 silicone phantom (150 mm by 100 mm), chosen to simulate abdominal tissue [11]. The force profiles were recorded with a Tedea Huntleigh 1040 (20 Kg) load cell and NI USB-6341 interface. The percussion force was found to range between 9 N and 11 N, the impulse between 0.7 and 0.8 Ns.

A. Vertical Spring and Mass System (Model 1)

The percussion action can be modelled as a spring-mass system. Let the spring constant be k and compression distance be x . Energy stored in the spring PE is:

$$PE = \frac{1}{2}kx^2 \quad (1)$$

When the compressed spring is released, the elastic energy is converted into kinetic energy:

$$\frac{1}{2}kx^2 = \frac{1}{2}mv_i^2 \quad (2)$$

$$v_i = \sqrt{\frac{kx^2}{m}} \quad (3)$$

where v_i is the initial velocity of the mass m .

It is assumed that the mass travels vertically downwards for a distance s until it hits the body surface. Let acceleration due to gravity be g . The velocity of the mass v_s when it hits the body is:

$$v_s^2 = v_i^2 + 2gs \quad (4)$$

$$v_s = \sqrt{\frac{kx^2}{m} + 2gs} \quad (5)$$

Let the deflection of the body be d , the deceleration of the mass a_s . Force exerted by the body F is then:

$$a = \frac{kx^2 + 2mgs}{2md} \quad (6)$$

$$F = ma = \frac{kx^2 + 2mgs}{2d} \quad (7)$$

This model shows the force exerted by the body can be controlled by varying the spring stiffness, compression distance and mass. The disadvantages of this model is the inability to control impact force and to retract the mass after first contact. When a human performs percussion, the finger rebounds after contact. A second model was designed to resolve this.

B. 2 Degrees of freedom linkage mechanism with compliant joints (Model 2)

By observing manual percussion, we found that the hand and forearm act as rigid links and the force at the finger tips originates from the elbow joint and is controlled by the wrist joint. Experienced doctors suggested to relax the wrist during percussion, implying controlling the stiffness of the wrist joint is key to effective percussion[12].

The arm and hand movement of one percussion action can be broken down in the following steps:

- 1) Elbow joint provides initial torque to the forearm and hands with the wrist joint being compliant.
- 2) When the hand is at a certain distance above the body, the forearm motion stops, and the hand continues to rotate around the wrist joint.
- 3) The finger tip impacts the surface and rebounds.
- 4) The examiner listens to the acoustic response and feels the haptic response with the resting hand.

To reflect this, the percussion arm can be modelled with lightweight rods connected with revolute joints as shown in Fig. 2. Two extension springs are used at the elbow joint for generating the initial torque to actuate the system and at the wrist joint for compliance control.

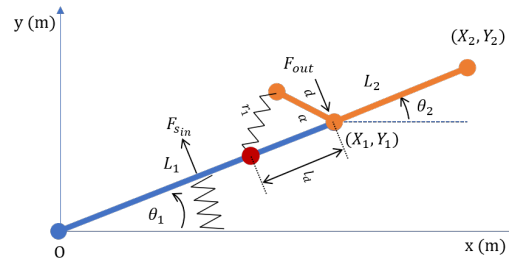


Fig. 2. Percussion arm model (Model 2). Blue: Forearm. Orange: Hand

The input force F_{in} is generated by extending the spring at the elbow joint:

$$F_{in} = k_e x_e \quad (8)$$

and the initial torque applied at the elbow joint (the origin) is:

$$\tau_e = F_{in} L_{in} = k_e x_e L_{in} \quad (9)$$

Where L_{in} is the input rod length, x_e is the extension of the elbow spring, and k_e is the elbow spring constant.

The wrist joint (X_1, Y_1) and end-effector (X_2, Y_2) positions can be calculated as follows:

$$X_1 = L_1 \cos(\theta_1) \quad (10)$$

$$Y_1 = L_1 \sin(\theta_1) \quad (11)$$

$$X_2 = L_1 \cos(\theta_1) + L_2 \cos(\theta_1 + \theta_2) \quad (12)$$

$$Y_2 = L_1 \sin(\theta_1) + L_2 \sin(\theta_1 + \theta_2) \quad (13)$$

where θ_1 is the elbow joint angle and θ_2 is the wrist joint angle.

The dynamics of the system is modelled using Lagrangian mechanics. The torques required to accelerate the limb inertia are expressed in terms of the mass matrix $\mathbf{H}(\theta)$, Coriolis and centrifugal forces $\mathbf{C}(\theta, \dot{\theta})$, and gravity $\mathbf{G}(\theta)$:

$$\begin{aligned} \mathbf{\tau}_B &= \mathbf{H}(\theta) \ddot{\theta} + \mathbf{C}(\theta, \dot{\theta}) + \mathbf{G}(\theta) \\ \mathbf{H}(\theta) &= \begin{bmatrix} H_{11} & H_{12} \\ H_{21} & H_{22} \end{bmatrix} \\ H_{11} &= I_1 + I_2 + m_1 L_{m1}^2 + m_2 (L_1^2 + L_{m2}^2 + 2L_1 L_{m2} c2) \\ H_{12} &= H_{21} = I_1 + m_2 L_{m2} (L_{m2} + L_1 c2) \\ H_{22} &= I_2 + m_2 L_{m2}^2 \\ \mathbf{C}(\theta, \dot{\theta}) &= \begin{bmatrix} -m_2 L_1 L_{m2} (2\dot{\theta}_1 \dot{\theta}_2 + \dot{\theta}_2^2) s2 \\ m_2 L_1 L_{m2} \dot{\theta}_1^2 s2 \end{bmatrix} \quad (14) \\ \mathbf{G}(\theta) &= \begin{bmatrix} (m_1 g L_{m1} + m_2 g L_1) c1 + m_2 g L_{m2} c12 \\ m_2 g L_{m2} c12 \end{bmatrix} \\ c1 &= \cos \theta_1, c2 = \cos \theta_2 \\ s1 &= \sin \theta_1, s2 = \sin \theta_2 \\ c12 &= \cos(\theta_1 + \theta_2), s12 = \sin(\theta_1 + \theta_2); \end{aligned}$$

where I_1, I_2 are inertia of the rods, m_1, m_2 are the mass of the rods, L_1, L_2 are full lengths of the rods, and L_{m1}, L_{m2} are distance to centre of mass of the rods.

The stiffness of the wrist joint can be adjusted by changing the pegging distance and the spring stiffness. The forearm rod L_1 was extended to include a hard stop to prevent the hand rod L_2 from over-bending, as shown in Fig. 3.

A beam of length d is attached at angle α to the hand rod. An extension spring with resting length r is attached to this connecting beam and the forearm rod, setting an initial pegging distance l_d . This distance can be adjusted by pulling the peg away from the wrist joint, resulting in a new pegging distance $l_d + x$ and spring length $r + \delta r$. As the joint rotates, the spring length changes as follows:

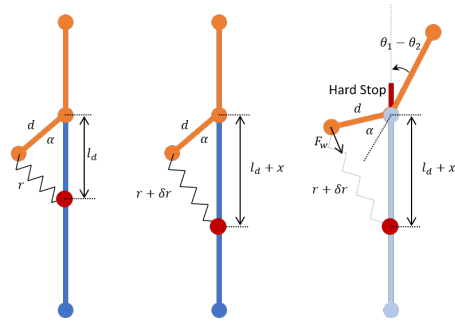


Fig. 3. Free-body diagram of the wrist joint (Model 2)

$$r + \delta r = \sqrt{(l_d + x)^2 + d^2 - 2d(l_d + x) \cos(a + \theta_1 - \theta_2)} \quad (15)$$

The spring pulling force is:

$$F_w = \delta r k_w \quad (16)$$

and the resultant torque around the wrist joint is:

$$\tau_w = F_w \frac{d \sin(a + \theta_1 - \theta_2)}{r + \delta r} (l_d + x) \quad (17)$$

The torque of the system at launch is:

$$\tau_s = \begin{bmatrix} \tau_e \\ \tau_w \end{bmatrix} = \begin{bmatrix} k_e x_e L_{in} \\ F_w \frac{d \sin(a + \theta_1 - \theta_2)}{r + \delta r} (l_d + x) \end{bmatrix} \quad (18)$$

The kinematics of the system is shown in Fig. 4. Once the elbow joint extension spring is at the minimum length, it stops L_1 moving further, the momentum is transferred to L_2 which makes impact with the tissue. Some assumptions and simplifications are made in this simulation:

- 1) The hard stop reverses and reduces the wrist joint velocity when L_2 is in contact, with a coefficient of restitution of 0.4.
- 2) When L_1 is stopped, kinetic energy of the system is transferred without loss to L_2 , and initial launch torque is removed.

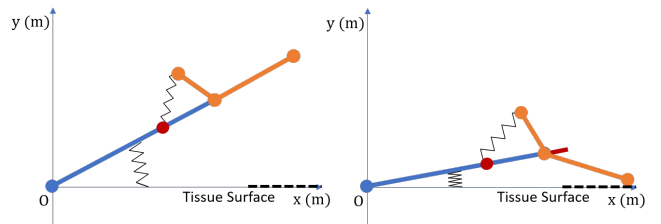


Fig. 4. Left: Release position. Right: First link stops, end-effector makes contact with tissue surface.

The analytical results showed that both elbow stiffness and wrist stiffness affect the force and impulse. The elbow spring stiffness has more influence on the maximum force exerted, and the wrist spring stiffness has more influence on impulse, as shown in Fig. 5. The model informed the design of a robotic actuator to replicate the percussion action.

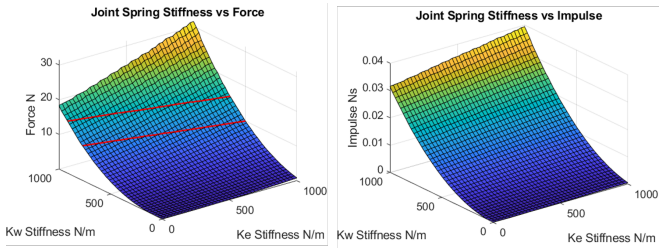


Fig. 5. Assume tissue deformation of 5 mm at impact. Ke is elbow spring stiffness and Kw is wrist spring stiffness. Left: elbow spring stiffness has a greater contribution to force. The region bounded by the two red lines matches with the human force profile. Right: wrist spring stiffness has a greater contribution to impulse, but is less than that of the human trial.

C. Hardware design and experimental set-up

This model was implemented into CAD (computer aided design) models using Fusion 360 (Fig. 6). The simulation results informed input design parameters to appropriately replicate the percussion action. The designs were additive manufactured using a Prusa MK3S. The cam is driven by a Tower Pro MG996R continuous servo motor, controlled by an Arduino Uno. Fig. 7 shows the force exerted by the tissue using this robotic percussion model, recorded using the same equipment that measured the human force, detailed previously. The force and impulse applied by the robotic model were found to be 8.5 N and 0.5 Ns respectively, determined to be appropriate in magnitude compared to the human and corroborating the analytical results.

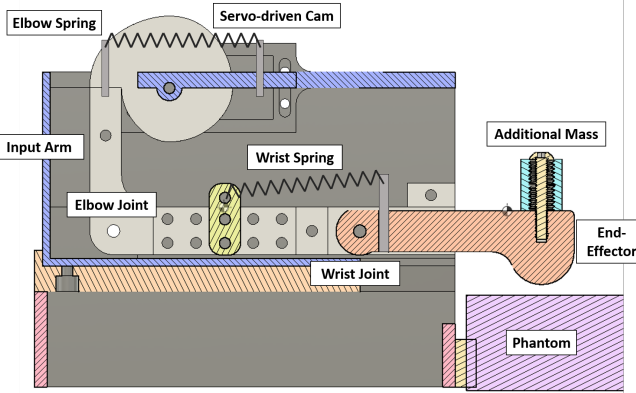


Fig. 6. CAD model of robotic percussion device. Additional mass can be added to the end-effector to adjust impact force

Representing a lipoma or cancerous lump, a nodule with a diameter of 11 mm was buried such that the phantom could be placed either way up, giving nodule depths of 2 mm and 15 mm (Fig. 8). A TIMESETL piezo-electric contact microphone was attached to the surface of the silicone phantom. It was positioned as close to the impact point as possible, making sure that clipping of the audio signal would not occur (shown in Fig. 9). The percussion device was programmed to record over 1000 datapoints for each side. Audio signal was transmitted with a Focusrite Scarlett 4i4 3rd Gen USB Audio Interface, and recorded with Audacity at 44100 Hz. The frequency range of interest

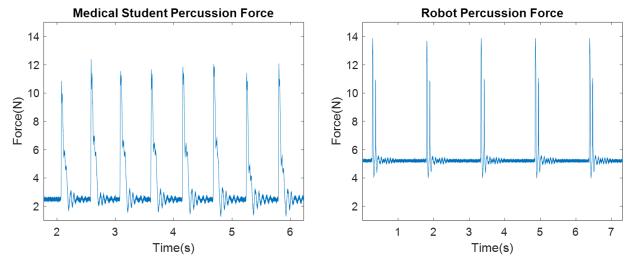


Fig. 7. Force readings of the human and robot performing percussion on the phantom. Human average force: 9 - 11 N, average impulse: 0.7 - 0.8 Ns. Robot average force: 8.5 N, average impulse: 0.5 Ns

is the human hearing range 20 Hz to 20000 Hz. Applying Nyquist's theorem, a minimum sampling frequency of 40000 Hz is required, hence a sampling frequency of 44100 Hz was chosen.

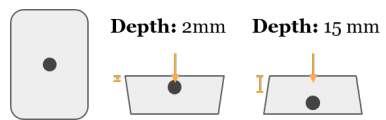


Fig. 8. Nodule depths of 2 mm ('close') and 15 mm ('far')

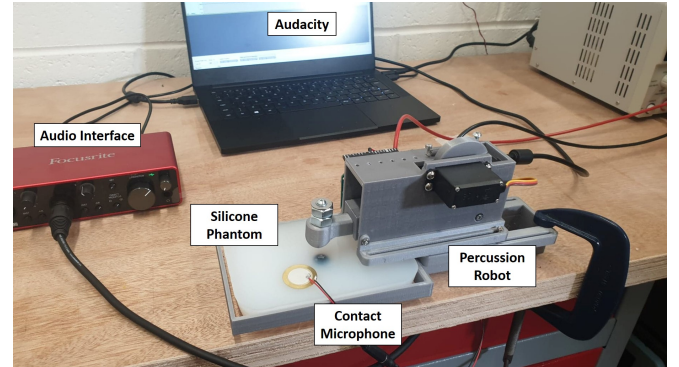


Fig. 9. Robotic percussion device experimental set-up

III. RESULTS

A. Signal Analysis Using Wavelet Transform

Signal processing was performed to understand how nodule depth affects the percussion-derived acoustic response. The raw signal was cropped to individual percussion events to find local maxima with specific peak prominence and distance. A total of 1,688 percussion events were extracted from 20 minutes of testing.

Savitzky-Golay filtering was employed to de-noise the signal whilst preserving maximum concurrence to the original signal (Fig. 10). Such filters are optimal at minimising the least-squares error when fitting a polynomial to frames of noisy data. Savitzky-Golay filters perform better in this application than standard averaging finite impulse response (FIR) filters, which tend to filter high-frequency content along with the noise. While Savitzky-Golay filters are less

successful at rejecting noise, preservation of high frequency signal components was a priority in this case.

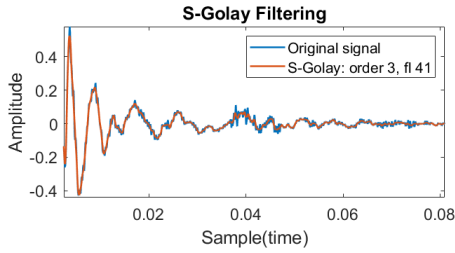


Fig. 10. Sample signal smoothing using Savitzky-Golay filtering.

The de-noised signal was analysed through a 1D Continuous Wavelet Transformations (CWT) coefficient scalogram. This was preferred over Fourier transformations as the time domain contained crucial information on time-localized spectral characteristics of the signal. The chosen mother wavelet family was Symlet (Sym) as the literature shows its wide use in audio analysis and signal damping [13][14][15].

The continuous wavelet transform $W(a, b)$ of the original signal $f(t)$ with respect to the Sym10 wavelet $\Psi(t)$ is:

$$W(a, b) = \int_{-\infty}^{\infty} f(t) \frac{1}{\sqrt{|a|}} \Psi * \frac{t-b}{a} dt \quad (19)$$

where a is the scale factor (determining resolution) and b is the time-localisation. The symbol $*$ denotes complex conjugation.

The scalogram in Fig. 11 shows the signal in time and frequency domain, as well as the coefficients C (colour bar). The coefficients C represent how closely correlated the wavelet is with this section of the signal. The larger the absolute value of C , the higher the similarity to the Symlet Wavelet at each time section and the higher the intensity. In order to compare the acoustic response from close and far nodule instances, an average of each group was generated and analysed. The resulting scalograms are shown in Fig. 11. The damping effect of close nodules is present, shown by faster-dying signal intensities Fig. 12 and higher intensities in the lower frequency bands of far nodules.

B. Higher Noise Levels of the Robotic Device

Using a robotic device to generate percussion actions minimises variations between motions. However, comparison of raw signal between human and the robotic device showed higher noise levels from the robotic percussion. The euclidean distance between different percussion event samples (Fig. 13) further confirm this (109.64 for the robotic device, 5.35 for the human).

Although the effect of noise is almost negligible at high amplitudes, it can affect the low-amplitude, reverberation waves. Fig. 14 exhibits de-phasing of the CWT decomposition waves. A possible cause is the lack of a pleximeter to absorb the energy of the plexor's strike; a pleximeter was not included in this study to simplify the experimental process. Noise was instead removed using computational filtering techniques.

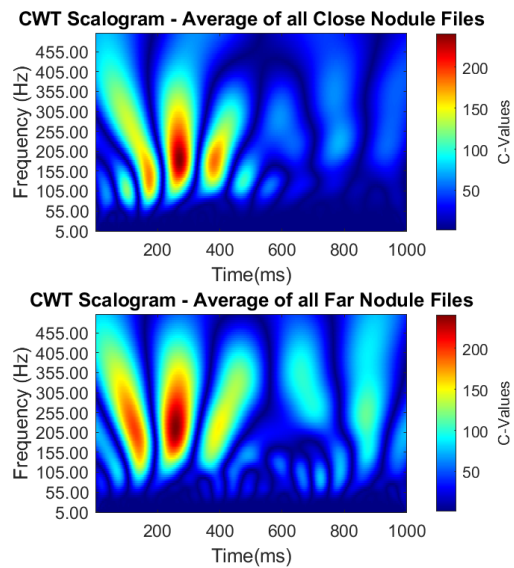


Fig. 11. Coefficient Scalograms for the average signal in close nodule (top) and far nodule (bottom) percussion instances. Graphs fitted to regions of interest (e.g. 5-500 Hz bands, max. frequency of raw signal is 1000 Hz).

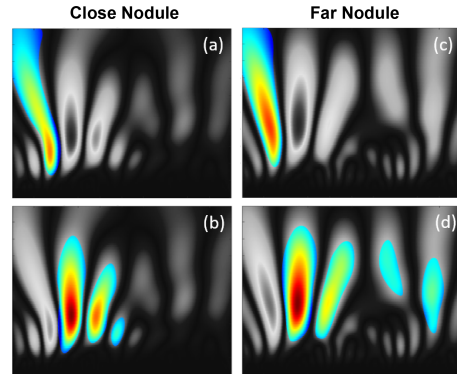


Fig. 12. (a) and (b) correspond to the close nodule scalograms, while (c) and (d) correspond to the far nodule data. (a) and (c) show a common high-intensity area during early time frames. This represents the device impact. The subsequent intensity areas highlighted in colour in (b) and (d) represent the acoustic response in the silicone phantom. These resonant waves diminish faster in the close nodule samples (b).

C. Signal Analysis Using A Convolutional Neural Network

Further signal analysis using a convolutional neural network (CNN) was motivated by a CNN's ability to be trained to ignore non-important data features (i.e. noise generated by the hardware) [16] and ability to create predictive models quantifiable with well-established metrics. In addition to this, the use of saliency maps makes it possible to visually identify areas of an input image that triggered the CNN's neurons when it correctly classifies an image. In this case, the input image is a spectrogram of a single percussion event [17]; the identified areas correspond to the key time-variant frequencies that differentiate the two datasets [18]. Spectrograms of each percussion event were saved as 3-channel 8-bit images and labelled with the relevant nodule depth (Fig. 15).

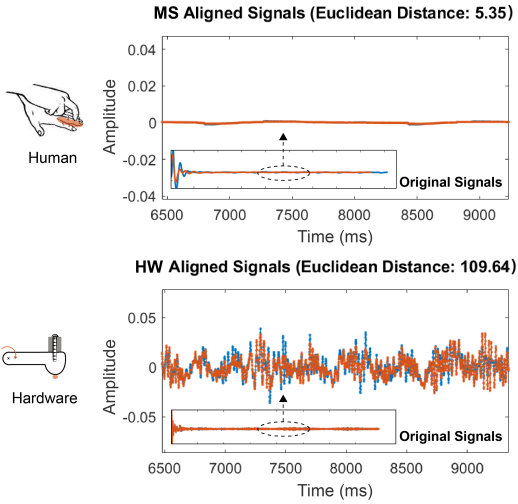


Fig. 13. Euclidean Distance between two different samples of close-nodule percussion events from the human (top) and the robotic device (bottom). A greater euclidean distance indicates discrepancies between samples, in this case higher noise levels in the robotic signal can be seen.

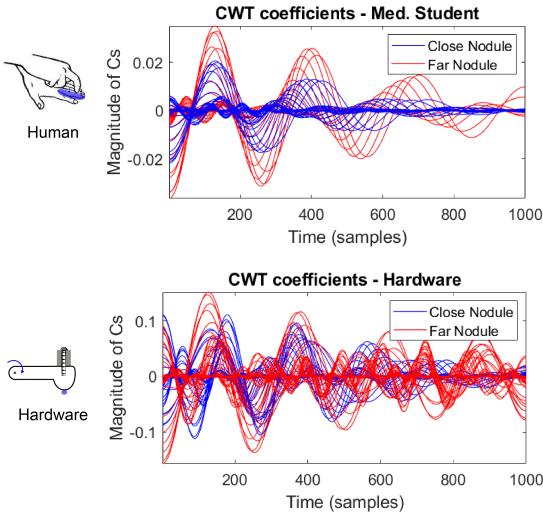


Fig. 14. C-values from 1D Continuous Wavelet Transformations using the Symlet family. CWT waves from the human (top) and the hardware device (bottom) suggest de-phasing due to noise.

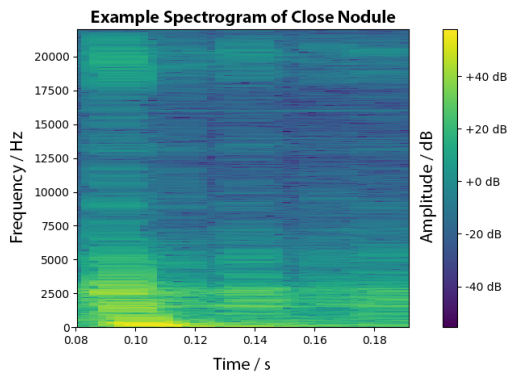


Fig. 15. A spectrogram of a single percussion event generated using the SciPy library. A spectrogram uses consecutive fourier transforms to plot the time variant frequency spectrum. A Tukey (tapered cosine) window with an overlap of 1/8th of the window length was used.

Spectral representations were chosen for their suitability for use with a CNN [19]. Spectral representations of audio signal retain more information than many hand-crafted features traditionally used for audio analysis, and are of lower dimension than raw audio. The CNN uses 4 layers with rectified linear activation functions together with max pooling and dropout regularisation (Fig. 16).

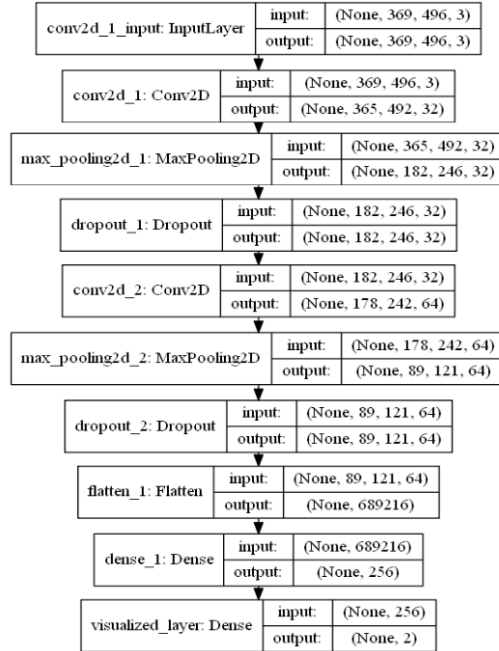


Fig. 16. Graphical representation of the architecture of the CNN. Dropout regularisation was used to reduce over-fitting.

Saliency maps are a weighted visual representation of the (salient) pixels that trigger the neurons in the CNN. This allowed for identification of areas that contribute to the CNN's underlying comprehension of the given images [18]. Saliency maps were generated for various spectrograms in order to evaluate the signal characteristics and validate the wavelet transform analysis.

IV. DISCUSSION

A. Tissue dynamics and acoustic response

Modelling the tissue as a mass-spring-damper in simulation enabled the exploration of the relationship between oscillation frequency and damping factor. The relationship between oscillation frequency and damping factor was found to be approximately linear (Fig. 17), suggesting that increasing the damping factor increases the oscillation frequency of the tissue. Our experimental results showed that the acoustic response of the tissue with a close nodule has a lesser low-frequency component (lower C-value magnitude), as such having a hard nodule closer to the surface of the tissue increases damping of the tissue. This, for the first time, shows that changes in the dynamic structure of a tissue model can be detected by a robotic percussion device and analysing its acoustic response. Hogan suggested that environment changes should be considered in manipulator control [20],

going forward it would be interesting to study whether doctors vary their joint stiffness to adapt to this change in tissue dynamics through acoustic feedback.

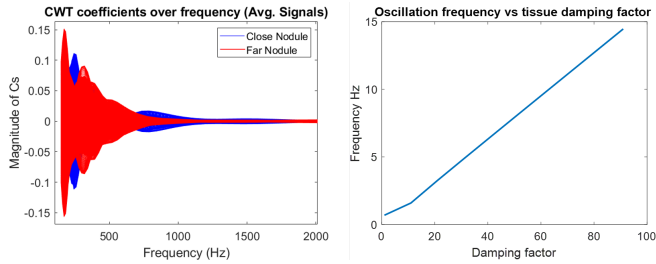


Fig. 17. Left: Magnitude of C-value in lower frequency regions of all close nodule signals are less than that of the far nodule signals. Right: Simulation results predict oscillation frequency of the spring-mass-damper model of the tissue increases linearly with damping factor. This suggests a close nodule leads to greater damping, as the C-value for the low-frequency regions of the close nodule tissue is smaller.

B. Analysis with a Convolutional Neural Network

Further signal analysis using saliency maps tested the hypothesis that a CNN would highlight the same frequencies of importance as the hand-crafted methods. The generated saliency maps suggest that the relevant or salient pixels are in the range of 0 kHz - 7.5 kHz and 15 kHz - 20 kHz. Consistency across the entire dataset, with minor variation, was found. Whilst saliency maps do not directly distinguish between the presence or absence of particular frequency bands, when comparing the spectrograms and saliency maps side-by-side it can be observed that the close nodule data shows an increase in amplitude in the higher-frequency band and decrease in the lower-frequency band. The smaller spread of the salient pixels along the time axis shows the lower frequencies are damped by the presence of the nodule, suggesting that both time and frequency domain analysis play an important role in classification. These findings concur with the insights gained from the wavelet transform analysis. This method of analysis using CNNs is novel in the study of percussion examination.

The CNN was able to identify the presence of a hard nodule in the silicone phantom with 100% accuracy in the experimental environment. Whilst this does not account for the significant variance inherent in examination on human subjects (patient physiology, nodule size, texture etc.), the method shows promise as an automated diagnostic tool in future work. However the experimental data was limited to 2 nodules and a significant amount of further data collection would be required to continue the development of the CNN. The proposed robotic device could be critical in streamlining and automating the data collection process, allowing the building of large data-sets that play to the strengths of deep learning techniques.

C. Statistical Hypothesis Testing

The statistical significance of the far nodule and close nodule data-sets was calculated to explore whether specific bands show a significant difference in intensity, allowing the

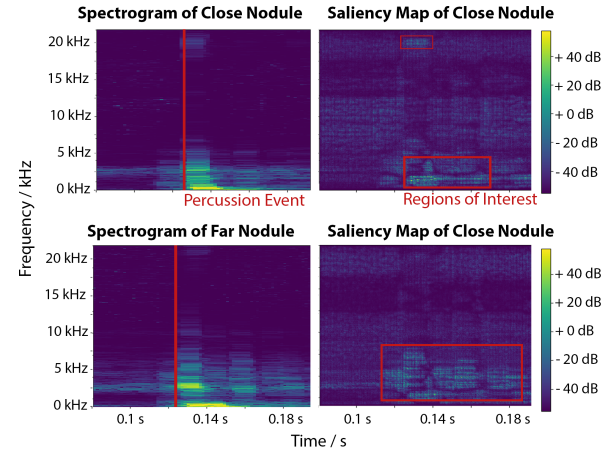


Fig. 18. Spectrograms for the close nodule (top left) and far nodule (bottom left) are shown in comparison with saliency maps from the final layer of the CNN for a single percussion data-point. Saliency maps show which areas of the input image triggered the CNN's neurons. Here the salient pixels show which time variant frequency amplitudes are used to classify the presence of a nodule. The important pixel values are outlined in red, with most of the relevant frequencies in the 200 to 2000 Hz range over 0.4s

qualitative insights gained from the proposed signal analysis work to be statistically quantified. The designed program performs multiple T-tests on the mean intensity of different frequency bands; a T-test was chosen so as to compare the means of the data-sets, assuming that the mean intensity of the frequency bands are normally distributed across the samples. A significance level of 0.01 was chosen.

The results of the T-tests (Table II) show that the change in frequency intensity between approximately 176 Hz and 300 Hz, 700 Hz to 2000 Hz, and 15500 Hz to 21000 Hz are statistically significant between the two data-sets. Other frequency bands showed lower statistical significance. Whilst each of these frequency bands show different amplitudes, the relative amplitude increase in the 176 Hz - 400 Hz band between the two nodule data-sets was much larger than the other bands, and is therefore more relevant to the experiment. When the frequency band was tested as the mean of its constituent frequencies, the p value was 0.001; when individual frequencies were tested independently, the p values ranged from 1.73E-05 to 6.00E-10. Additionally, there was a statistically significant distance in the frequency band between 15600 Hz and 21100 Hz with a p value of 3.76E-08. These results report that the work outlined in this paper has statistical significance and the proposed hypothesis is accepted.

Fig. 19 shows the most statistically significant region between frequency bands 7 (175 Hz - 200 Hz) and 16 (400 Hz , 425 Hz), which correlates to the values in Table II.

D. Limitations

The proposed method showed rigorous analysis of results of a controlled experiment, however in reality percussion examination is far from a controlled environment. The size and shape of the silicone phantom used in this experiment is not representative of the human abdominal region. Some of

TABLE II

T-TEST RESULTS FOR THE MOST RELEVANT FREQUENCY BANDS.

Frequency Band / Hz	Statistically Significant	P - Value
0-176	False	0.02015
176-400	True	2.9391E-176
500 - 700	False	0.3201
700 - 2000	True	1.38158E-04
2000 - 15500	False	0.6909
15500 - 21000	True	3.76940E-08
21000 - 22000	False	0.8774

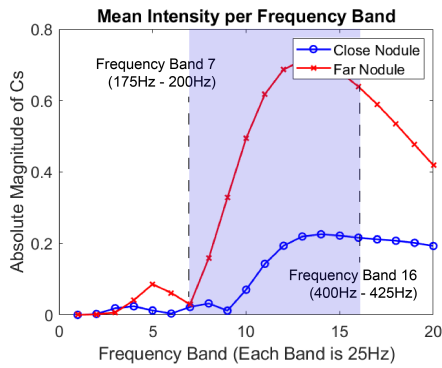


Fig. 19. Absolute, mean C-values of frequency bands. Highlighted in blue is the most statistically significant frequency bands region.

the detected acoustic response characteristics may be due to the phantom's dimensions and not be present in a patient. The silicone phantom does not account for the variation between patients; the human abdomen is a complex structure consisting of layers of tissues with different mechanical properties, and the nodule may be embedded in a variety of layers, resulting in different acoustic responses. Whilst the use of a silicone phantom to simulate *palpation* of a nodule is established in the literature [11], its effectiveness in simulating *percussion* has not been studied.

This experiment did not consider the impact of the haptic (non-audio) response, and ignored the influence of the pleximeter (non-percussing) hand. In absorbing and distributing the energy of the plexor, it is possible the pleximeter hand has noise attenuating qualities. This paper proposes an initial exploration into the field, and there is significant scope for further experimentation, expanding upon the the simplifications made here.

V. CONCLUSION

In this paper, a robotic device to replicate manual percussion was developed. Following analytical insights from simulation of the widely-used manual percussion method, a novel actuation mechanism was designed. A compliant joint provided an accurate recreation of the percussion action. The robotic device showed comparable force and impulse profiles to a human participant when performing percussion, with better consistency between percussion actions. Tests were performed on a silicone phantom with a buried hard nodule to simulate a lipoma (or cancerous lump) of the abdomen. Wavelet transform analysis reported clear differ-

ences in acoustic response between the percussion of a close (2 mm depth) nodule and a far nodule (15 mm depth). Saliency maps confirmed that a convolutional predictive model distinguished the same difference. Higher intensity frequencies between 176 Hz and 400 Hz were observed with the close nodule and this hypothesis was accepted following statistical testing. A qualitative assessment of scalogram and spectrogram visualisations suggested that the close nodule in the tissue model causes a detectable increase in damping. The proposed method, for the first time, provides design guidelines for how a robotic device and audio analysis might be used to aid or automate percussion examination. Future studies will explore whether these results are reported in a more representative abdomen model or in human participants.

REFERENCES

- [1] D. C. Hall, M. K. Goldstein, and G. H. Stein, "Progress in manual breast examination," *Cancer*, vol. 40, no. 1, pp. 364–370, 1977.
- [2] J. B. P. Barth and H. Roger, *Traité pratique d'auscultation; suivi d'un précis de percussion*. Labé, 1860.
- [3] S. E. D. JoVE. (2020) Physical examinations ii. abdominal exam ii: Percussion. [Online]. Available: <https://www.jove.com/science-education/10090/abdominal-exam-ii-percussion>
- [4] J. C. Yernault and A. Bohadana, "Chest percussion," *European Respiratory Journal*, vol. 8, no. 10, pp. 1756–1760, 1995.
- [5] A. Harris, "Listening-touch, affect and the crafting of medical bodies through percussion," *Body & society*, vol. 22, no. 1, pp. 31–61, 2016.
- [6] L. A. (1722-1809). Percusor and pleximeter, image ref:10289197.
- [7] J. S. Thierman, "Device for medical percussion," Sep. 14 2004, uS Patent 6,790,184.
- [8] D. A. Rice, "Transmission of lung sounds," in *Seminars in respiratory medicine*, vol. 6, no. 03. Copyright© 1985 by Thieme Medical Publishers, Inc., 1985, pp. 166–170.
- [9] V. A. McKusick, J. T. Jenkins, and G. N. Webb, "The acoustic basis of the chest examination: studies by means of sound spectrography," *American review of tuberculosis*, vol. 72, no. 1, pp. 12–34, 1955.
- [10] H. Mansy, T. Royston, and R. Sandler, "Use of abdominal percussion for pneumoperitoneum detection," *Medical and Biological Engineering and Computing*, vol. 40, no. 4, pp. 439–446, 2002.
- [11] M. Li, J. Konstantinova, G. Xu, B. He, V. Aminzadeh, J. Xie, H. Wurdemann, and K. Althoefer, "Evaluation of stiffness feedback for hard nodule identification on a phantom silicone model," *PloS one*, vol. 12, no. 3, 2017.
- [12] Lusignan, "Robopatient meeting, university of oxford," 2020.
- [13] Z. X. Diqun Yan, Li and R. Wang, "Detection of hmm synthesized speech by wavelet logarithmic spectrum," *Automatic Control and Computer Sciences*, vol. 53, no. 1, pp. 72–79, 2019.
- [14] O. A. Naït-Ali, A. and J. Motsch, "Modelling and recognition of brainstem auditory evoked potentials using symlet wavelet," *IRBM*, vol. 21, no. 3, pp. 150–157, 2000.
- [15] M. Y. O. G. P. J.-M. Misiti, M., "Wavelet toolbox user's guide," *Natick, MA: The MathWorks, Inc*, vol. 21, no. 3, pp. 139–145, 674, 2009.
- [16] M. Kozierski and B. Cyganek, "Image recognition with deep neural networks in presence of noise—dealing with and taking advantage of distortions," *Integrated Computer-Aided Engineering*, vol. 24, no. 4, pp. 337–349, 2017.
- [17] A. Miller, B. Blott et al., "Review of neural network applications in medical imaging and signal processing," *Medical and Biological Engineering and Computing*, vol. 30, no. 5, pp. 449–464, 1992.
- [18] H. Li, Y. Tian, K. Mueller, and X. Chen, "Beyond saliency: Understanding convolutional neural networks from saliency prediction on layer-wise relevance propagation," *Image and Vision Computing*, vol. 83-84, p. 70–86, Mar 2019.
- [19] L. Wyse, "Audio spectrogram representations for processing with convolutional neural networks," 2017.
- [20] N. Hogan, "Impedance control: An approach to manipulation," in *1984 American control conference*. IEEE, 1984, pp. 304–313.